Magnetic properties and signatures of moment ordering in the triangular lattice antiferromagnet KCeO$_2$

Mitchell M. Bordelon,[1] Xiaoling Wang [ORCID],[2] Daniel M. Pajerowski,[3] Arnab Banerjee [ORCID],[4] Mark Sherwin,[2] Craig M. Brown [ORCID],[5,6]
M. S. Eldeeb,[7] T. Petersen [ORCID],[7] L. Hozoi,[7] U. K. Rößler [ORCID],[7] Martin Mourigal [ORCID],[8] and Stephen D. Wilson [ORCID][1,*]

[1]*Materials Department, University of California, Santa Barbara, California 93106, USA*
[2]*Department of Physics and Center for Terahertz Science and Technology,*
University of California, Santa Barbara, California 93106, USA
[3]*Neutron Scattering Division, Oak Ridge National Laboratory, Oak Ridge, Tennessee 37831, USA*
[4]*Department of Physics, Purdue University, West Lafayette, Indiana 47906, USA*
[5]*Department of Chemical and Biomolecular Engineering, University of Delaware, Newark, Delaware 19716, USA*
[6]*Center for Neutron Research, National Institute of Standards and Technology, Gaithersburg, Maryland 20899, USA*
[7]*Institute for Theoretical Solid State Physics, Leibniz IFW Dresden, Helmholtzstrasse 20, 01069 Dresden, Germany*
[8]*School of Physics, Georgia Institute of Technology, Atlanta, Georgia 30332, USA*

The magnetic ground state and the crystalline electric field level scheme of the triangular lattice antiferromagnet KCeO$_2$ are investigated. Below $T_N = 300$ mK, KCeO$_2$ develops signatures of magnetic order in specific heat measurements and low energy inelastic neutron scattering data. Trivalent Ce^{3+} ions in the D_{3d} local environment of this compound exhibit large splittings among the lowest three $4f^1$ Kramers doublets defining for the free ion the $J = 5/2$ sextet and a ground state doublet with dipole character, consistent with recent theoretical predictions by Eldeeb *et al.* [Phys. Rev. Materials **4**, 124001 (2020)]. An unexplained, additional local mode appears, and potential origins of this anomalous mode are discussed.

DOI: 10.1103/PhysRevB.104.094421

I. INTRODUCTION

Magnetically frustrated materials provide unique settings for realizing new electronic phases of matter. For instance, the triangular lattice antiferromagnet has been a prime platform for searching for highly entangled, quantum spin liquid (QSL) states and other unconventional ground states [1–6]. Antiferromagnetic nearest neighbor interactions across a triangular lattice network can preclude conventional magnetic order, depending on the strength of quantum fluctuations and exchange anisotropies. In the Heisenberg limit, the ground state of the nearest neighbor triangular lattice antiferromagnet is a three-sublattice order with moments rotated 120° relative to one another across a single triangle [7–9]. However, strong quantum fluctuations associated with small $S_{eff} = 1/2$ moments combined with strong anisotropies can instead favor a fluctuating QSL ground state such as the two-dimensional Dirac quantum spin liquid [3,10–12] or "resonating valence bond" states [13–18].

While the triangular lattice is a relatively common lattice motif, few materials show signatures of hosting intrinsically quantum disordered magnetic ground states. Recently, several rare earth, Yb-based oxides were reported to form quantum disordered ground states, with prominent examples being YbMgGaO$_4$ [16–27] and NaYbX$_2$ (X = chalcogenide) [11,28–36]. These and related materials do not form long-range magnetic order and instead display continuum spin excitations and thermodynamic properties consistent with QSL ground states.

One of the appeals of using rare earth moments in strong ligand fields to explore the states possible within a triangular lattice is the ability to vary the character (e.g., anisotropies) of the resulting $S_{eff} = 1/2$ moments via chemical substitution. Altering the rare earth ions can change moment size, *g*-factor anisotropy, exchange anisotropy, as well as the nature of the ground state multiplet. For example, swapping Tm^{3+} for Yb^{3+} in the YbMgGaO$_4$ structure results in multipolar, three-sublattice order [37–39]. Another recent rare earth QSL candidate, NaYbO$_2$, is a member of a much larger series of ARX_2 (A = alkali, R = rare earth, X = chalcogenide) compounds, and a large number of these compounds with varying R sites crystallize within the same $R\bar{3}m$ triangular lattice structure [11,28–36,40–46]. This invites exploration of the effect of tuning the character of the R-site magnetic ion in NaYbO$_2$ and exploring the response on its quantum disordered ground state.

Here we report a study of the single f-electron, Ce-based analog of NaYbO$_2$ in the triangular lattice antiferromagnet KCeO$_2$. This compound possesses $S_{eff} = 1/2$ moments with a large g factor anisotropy—one where the strong crystalline electric field surrounding trivalent Ce^{3+} ions is on the same order of magnitude as the Ce ion's spin-orbit coupling strength. We observe thermodynamic signatures of magnetic ordering, and, surprisingly, we also observe a well-separated extra excitation that cannot be explained by

---

*stephendwilson@ucsb.edu

traditional models of the Ce^{3+} $J = 5/2$ ground state multiplet. We propose a crystalline electric field scheme consistent with a recently reported *ab initio* model [47] and discuss the potential origins of the additional anomalous f-electron mode.

II. METHODS

A. Sample preparation

$KCeO_2$ was prepared by reducing CeO_2 with potassium metal adapted from a previous report [48]. A 1.1:1.0 molar ratio of K (99.95% Alfa Aesar) and CeO_2 (99.99% Alfa Aesar) was sealed in 316 stainless steel tubing inside of an Ar filled glove box following similar syntheses of $NaCeO_2$ and $NaTiO_2$ [49,50]. The sealed stainless steel tubes were placed in an actively pumped vacuum furnace at 800 °C for three days and opened in the glove box, revealing a highly air and moisture sensitive red-brown powder. All subsequent measurements were obtained with strict atmospheric control of the sample. Sample composition was verified via x-ray diffraction measurements under Kapton film on a Panalytical Empyrean powder diffractometer with Cu-Kα radiation, and data were analyzed using the Rietveld method in the Fullprof software suite [51] and GSAS/EXPGUI programs [52,53]. Powder samples were made in 5g batches. At most, only two batches were combined for powder neutron scattering experiments, where, prior to mixing, the samples were checked for quality and composition via x-ray diffraction and then thoroughly ground together.

B. Magnetic susceptibility, heat capacity, and electron paramagnetic resonance

Magnetic properties of $KCeO_2$ were collected using a Quantum Design magnetic properties measurement system (MPMS3) with a 7 T magnet and a Quantum Design physical properties measurement system (PPMS) with a 14 T magnet and vibrating sample magnetometer. Zero field cooled (ZFC) and field cooled (FC) magnetic susceptibility of $KCeO_2$ from 2 K to 300 K were measured in the MPMS3 under an applied field of $\mu_0 H = 0.5$ T. Isothermal magnetization data were collected at 2, 10, 100, and 300 K in the PPMS in fields up to $\mu_0 H = 14$ T. Heat capacity was measured from 2 K to 300 K in the PPMS. At lower temperatures, heat capacity data were collected using a dilution refrigerator insert within the PPMS between 80 mK and 4 K in external fields of $\mu_0 H = 0, 9,$ and 14 T. Electron paramagnetic resonance (EPR) spectra were collected at 4 K in an X-band EMXplus (Bruker) EPR spectrometer in the perpendicular operation mode, and data were modeled with the EasySpin package implemented in MATLAB [54].

C. Neutron scattering

Neutron powder diffraction data were collected on the high-resolution powder diffractometer BT-1 at the National Institute of Standards and Technology (NIST) Center for Neutron Research (NCNR). The sample was loaded in a ^{3}He cryostat and dilution refrigerator as pressed pellets in a copper can pressurized with He gas, and data were collected with incident neutrons of wavelength 2.0774 Å using a Ge(311) monochromator. Structural analysis was performed with Rietveld refinement using the GSAS/EXPGUI program [52,53]. Low-energy inelastic neutron scattering (INS) data were collected using 10 g of $KCeO_2$ powder at the Cold Neutron Chopper Spectrometer (CNCS) instrument at the Spallation Neutron Source, Oak Ridge National Laboratory (ORNL). The sample was loaded as pressed pellets into an 8 T cryomagnet with a dilution insert in a copper can with He exchange gas, and data were collected using incident neutrons of $E_i = 3.32$ meV. The magnet and instrument background were approximated by subtracting empty copper can scans at 1.8 K. High-energy INS data were collected at the wide Angular-Range Chopper Spectrometer (ARCS) at the Spallation Neutron Source. 5 g of powder were loaded within an aluminum can closed-cycle refrigerator and data were collected at 5 K and 300 K. Two incident energies of $E_i = 300$ meV (Fermi 1, Fermi frequency 600 Hz) and $E_i = 600$ meV (Fermi 1, Fermi frequency 600 Hz) were used, and background contributions were removed by measuring an empty sample can at the same incident energies and temperatures.

D. *Ab initio* modeling

Modeling of the energy spectrum of defect states in $KCeO_2$ was performed using complete active space self-consistent field (CASSCF) quantum chemical computations [55] including spin-orbit coupling (CASSCF + SOC). An embedded-cluster material model was employed. With this approach, electronic-structure calculations are carried out just for a finite set of atoms (i.e., a cluster), while the remaining part of the extended crystalline surroundings is described as an effective electrostatic field. For the type of defect we focused on, a Ce^{3+} ion within the K layer, a $[(CeO_6)Ce_{12}K_6]$ cluster was considered.

Effective core potentials and valence basis sets as optimized in Refs. [56,57] were used for the 'central' Ce ion at the 3b crystallographic position, along with all-electron $[4s3p2d]$ Douglas-Kroll basis sets for the adjacent ligands [58]. The positions of the latter were not reoptimized. To model the charge distribution in the immediate vicinity, we relied on large-core relativistic pseudopotentials including the $4f$ electrons in the core as concerns the twelve Ce nearest neighbors [59,60] and on total-ion potentials as concerns the six adjacent K sites [61]. Charge neutrality was ensured through distributing a negative charge of -2 e at metal sites far away from the defect Ce ion sitting at a 3b K site. An active space defined by the seven Ce $4f$ orbitals was used in the CASSCF computation. The latter was performed for an average of the seven $4f^1$ $S = 1/2$ states. Spin-orbit coupling was subsequently accounted for according to the procedure described in Ref. [62]. The quantum chemical package MOLPRO [63] was employed for these simulations.

III. EXPERIMENTAL RESULTS

A. Structural and bulk electronic properties

Neutron diffraction data was collected at 300 mK and the refined crystallographic parameters are shown in Fig. 1 and Table I. The $R\bar{3}m$ structure of $KCeO_2$ was previously reported at room temperature [48], and this was used as a starting point for the lattice refinement. No chemical site-mixing or
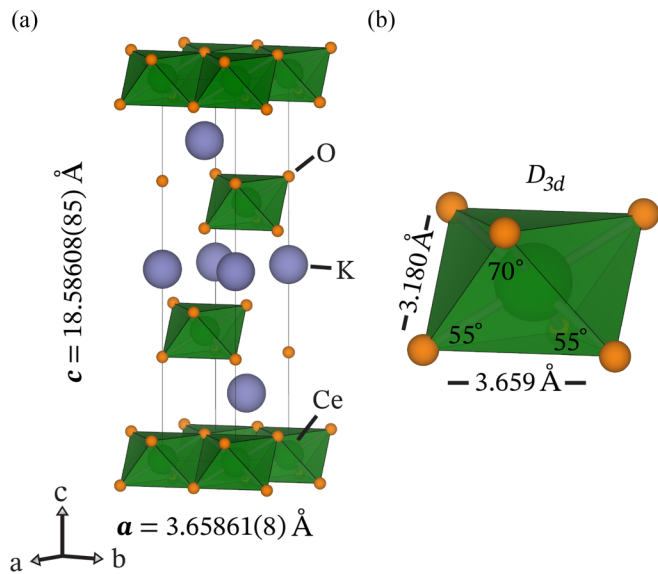
FIG. 1. (a) Experimentally determined lattice parameters and $R\bar{3}m$ crystal structure of $KCeO_2$ at 300 mK. Layers of K ions (purple) separate triangular sheets of CeO_6 octahedra. (b) The CeO_6 octahedra are trigonally compressed along the crystallographic c axis, resulting in a D_{3d} symmetry local environment about the Ce ions.

vacancies were observed in our analysis to within experimental resolution (~1%). As illustrated in Fig. 1, there is a sizable trigonal distortion in this material, which will be discussed later when the crystalline electric field level structure is examined. Furthermore, no magnetic Bragg peaks appear in the refinement at 300 mK, and additional measurements performed at 90 mK similarly failed to resolve magnetic scattering (Fig. 2). The difference between 90 mK and 5K diffraction data is shown in Fig. 1(c).

Specific heat measurements were collected under external magnetic fields of $\mu_0 H = 0$, 9, and 14 T at temperatures ranging from 80 mK to 300 K. The data are presented in Fig. 3, and two features appear below 10 K. The first is a broad peak centered near $T = 3$ K that shifts to higher temperatures with increasing magnetic field strengths and likely indicates the onset of short-range correlations. The second, sharper peak is centered at $T_N = 300$ mK and is suggestive of the onset of long-range magnetic order. Upon increasing the applied

TABLE I. Rietveld refinement of structural parameters at 300 mK from elastic neutron scattering data on BT-1. Within error, all ions refine to full occupation and no site mixing is observed. Reduced $\chi^2 = 5.23$.

T				300 mK		
$a = b$				3.65861(8) Å		
c				18.58608(85) Å		
Atom	Wyckoff	x	y	z	U_{iso} (Å^2)	Occupancy
Ce	3a	0	0	0	0.84(11)	0.994(5)
K	3b	0	0	0.5	1.09(15)	0.992(7)
O	6c	0	0	0.26939(11)	0.97(8)	0.999(5)

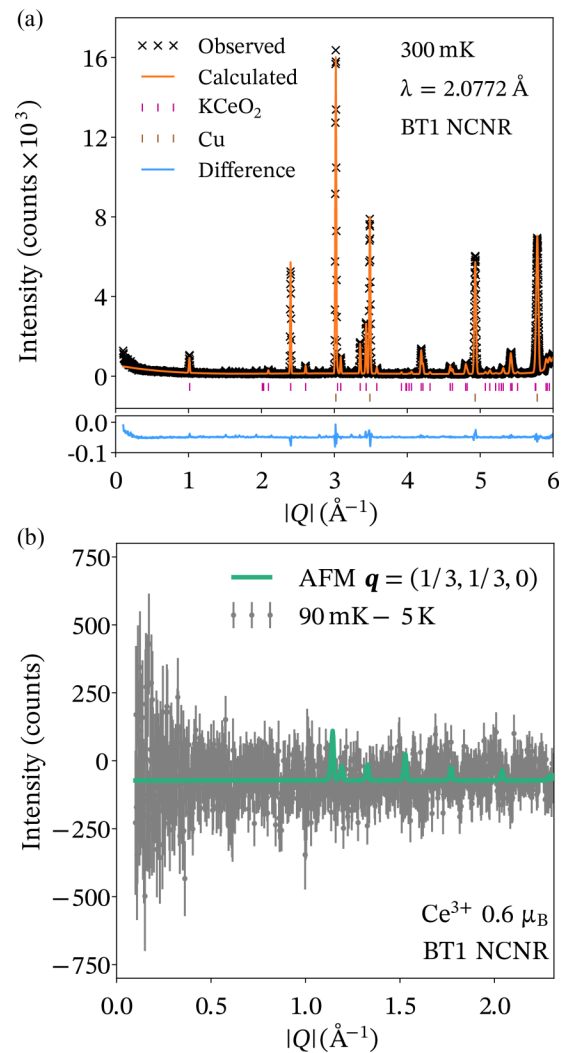FIG. 2. (a) Powder neutron diffraction data of $KCeO_2$ collected at 300 mK on the BT-1 diffractometer. No new magnetic reflections are resolved at 300 mK. Solid line shows the results of Rietveld refinement of the data and the lower panel shows the difference between the model and the data. (b) 90 mK diffraction data with high temperature (5 K) background subtracted and collected in a dilution refrigerator. The solid green line shows a simulated diffraction pattern for $\mathbf{q}=(1/3, 1/3, 0)$ 120° type order with 0.6 μ_B per Ce site. It is meant to provide a visual benchmark for the detection limit of magnetic order.

magnetic field, the $T_N = 300$ mK anomaly softens and shifts to lower temperatures as the Ce moments begin to polarize.

To further explore the magnetism at low temperature, magnetic susceptibility and isothermal magnetization measurements were performed. The resulting data are presented in Fig. 4. The inverse susceptibility is linear between 2 K to 300 K and was fit to a Curie-Weiss form, yielding antiferromagnetically coupled ($\Theta_{CW} = -7.7$ K) $\mu_{eff} = \sqrt{8C} = 1.22$ μ_B Ce moments. This corresponds to a powder-averaged g_{avg} factor of $g_{avg} = \mu_{eff}/[\sqrt{J_{eff}(J_{eff} + 1)}] = 1.41$ assuming $S_{eff} = 1/2$ Ce moments. Isothermal magnetization data collected at select temperatures are also plotted in Fig. 4(b) and show an approximately linear response from 0 to 14 T. We note that some high-field curvature appears in the 2 K data
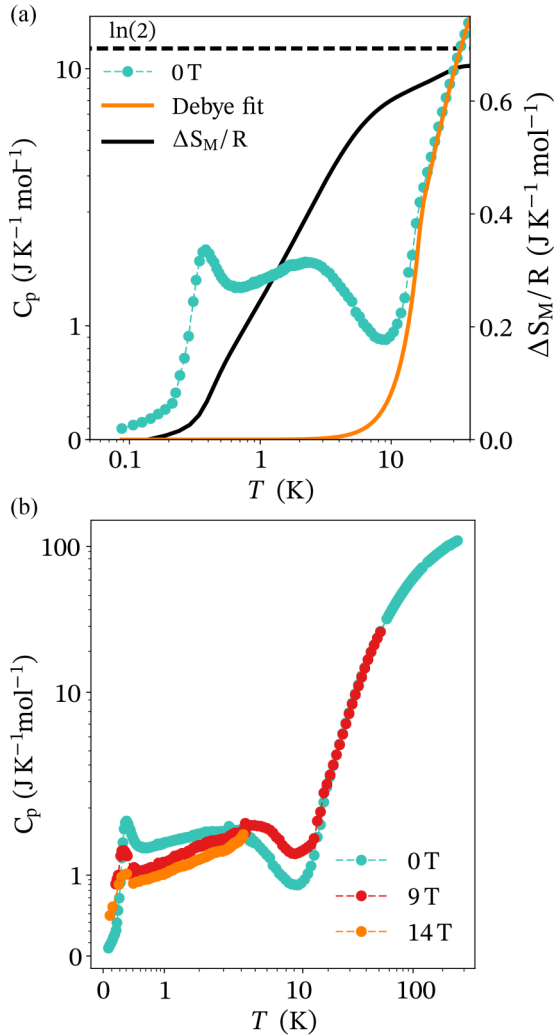
FIG. 3. (a) Specific heat $C_p(T)$ of KCeO$_2$ (cyan) measured in zero magnetic field and plotted with a Debye fit (orange) modeling lattice contributions. The magnetic specific heat peaks at 300 mK, suggesting KCeO$_2$ enters an ordered state. The integrated magnetic entropy is overplotted as a black line and approaches $R\ln(2)$ at high temperature (indicated by the horizontal dashed black line). (b) $C_p(T)$ of KCeO$_2$ collected under fields of $\mu_0 H = 0, 9$, and 14 T.

as the expected saturated magnetization of ~ 0.7 μ_B/Ce ion is approached.

Electron paramagnetic resonance (EPR) data were also collected and are plotted in Fig. 4(c). A highly anisotropic g factor is observed and the signal contains one sharp resonance corresponding to $g_\perp = 1.992 \pm 0.001$ and $g_\parallel = 0.32$. Broadening of this EPR line shape was attributed to a normal distribution of $g_{//}$ with full width at half maximum (FWHM) of 0.1. These g factor components indicate $g_{\text{avg}} = \sqrt{1/3(g_{//}^2 + 2g_\perp^2)} = 1.63 \pm 0.01$, which is slightly larger than that fit from the inverse susceptibility value. Since EPR is a more direct measurement of the g-factor tensor, these EPR values are later used to help model the crystalline electric field level structure.

B. Crystalline electric field excitations

Inelastic neutron scattering data are presented in Fig. 5 with an incident energy $E_i = 300$ meV. An uncommonly large splitting of the $J = 5/2$ multiplet is observed in Fig. 5(a), with the first excited state appearing near 118 meV—an energy of similar magnitude to the spin orbit coupling strength. The high energy of the crystal field validates our earlier use of the Curie-Weiss model up to 300 K. Specifically, three sharp excitations with energy widths limited by the resolution of the measurement were observed at $E_1 = 118.8 \pm 8.0$ meV, $E_2 = 146.2 \pm 6.9$ meV, and $E_3 = 170.5 \pm 6.1$ meV where error bars represent the full width at half maximum (FWHM) energy resolution of the instrument (FWHM at $E = 0$ is 12.8 meV). Data collected with a larger $E_i = 600$ meV show excitations into the $J = 7/2$ multiplet with transitions at $E_3 = 280 \pm 18$ meV, $E_4 = 370 \pm 14$ meV, and $E_5 = 440 \pm 12$ meV, consistent with the expected spin-orbit coupling strength of Ce^{3+}, and revealing three of the four expected $J = 5/2$ to $J = 7/2$ intermultiplet transitions. To analyze the splitting within the $J = 5/2$ multiplet, Q-averaged cuts through $I(\mathbf{Q}, \hbar\omega)$ are plotted as a function of energy from the $E_i = 300$ meV data shown in Fig. 5(b). The spectral weights of peaks from this cut were utilized to analyze the CEF level structure.

Notably, within this lower energy data, there is one extra mode beyond those expected for excited doublets within the $J = 5/2$ multiplet. The trivalent Ce^{3+} ions ($4f^1$, $L = 3$, $S = 1/2$) in KCeO$_2$ reside in a local environment with D_{3d} symmetry and total angular momentum $J = |L - S| = 5/2$ according to Hund's rules. In D_{3d} symmetry, the $J = 5/2$ manifold is maximally split into three CEF doublets following Kramers theorem, which should render only two excitations in the INS spectrum. The crystalline electric field level scheme for KCeO$_2$ was recently calculated by *ab initio* modeling by Eldeeb *et al.* [47], and this prediction provides a useful starting point for analyzing the neutron scattering data. To identify the origin of the extra mode, we reference the multireference configuration interaction with spin-orbit coupling (MRCI + SOC) calculations that predict two $J = 5/2$ intramultiplet excitations near $E = 121$ meV and $E = 143$ meV, and the first $J = 7/2$ intermultiplet excitation near $E = 252$ meV. The INS data are in close correspondence to this level structure, establishing the $E_3 = 170.5$ meV mode as the anomalous outlier. Therefore, for the purposes of analyzing the CEF ground state, the E_3 mode was not utilized to fit the CEF Hamiltonian. The origin of this mode is currently unknown and is discussed in further detail in later paragraphs.

Using the parameterized E_1 and E_2 excitations, the neutron data can be fit to model the CEF Hamiltonian. A D_{3d} Hamiltonian of CEF parameters B_n^m and Steven's operators $\hat{O}_m^n$ [64] becomes:

$$H_{\text{CEF}} = B_2^0 \hat{O}_2^0 + B_4^0 \hat{O}_4^0 + B_4^3 \hat{O}_4^3. \quad (1)$$

The CEF Hamiltonian was diagonalized in the CEF interface of Mantid [65] to determine energy eigenvalues and eigenvectors of the $J = 5/2$ excited states. Intramultiplet transition probabilities and g tensor components were calculated from the resulting wave functions. These values were then fit to integrated intensity ratios of the two excitations in the
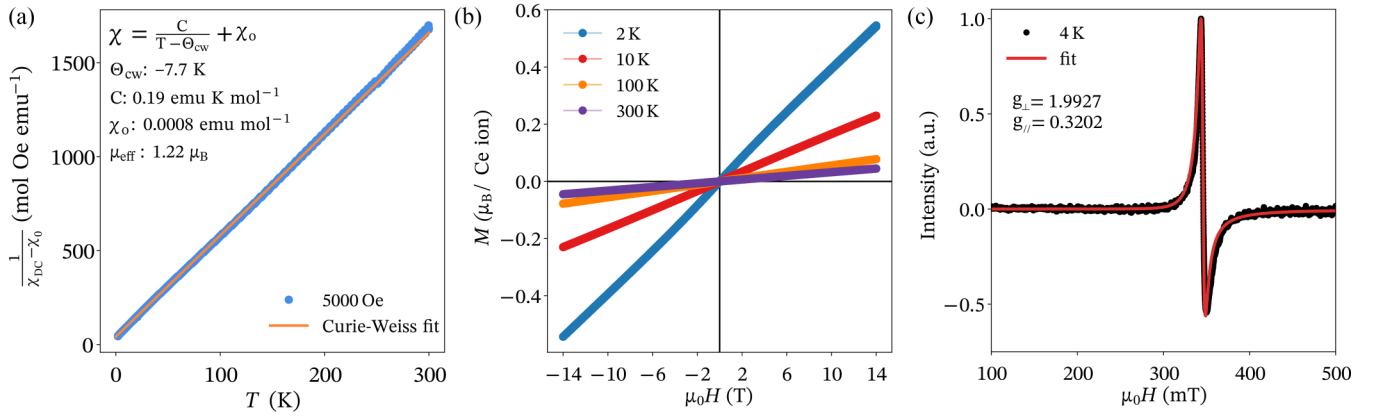
FIG. 4. (a) Inverse magnetic susceptibility of $KCeO_2$ collected under 0.5 T and overplotted with a Curie-Weiss fit to the data. (b) Field dependence of isothermal magnetization at 2, 10, 100, and 300 K. (c) EPR data collected at X-band and 4 K fit to a highly anisotropic g factor of $g_\perp = 1.9927$ and $g_{//} = 0.3202$. 1 emu mol^{-1} $Oe^{-1} = 4\pi\ 10^{-6}$ m^3 mol^{-1}.

INS data and the g-factor components from EPR data by following the minimization procedure reported in Bordelon *et al.* [40]. The results are presented in Table II, and the final fit of the CEF scheme contains a superposition of $m_j = 1/2$ and $m_j = 5/2$ angular momentum states that yield anisotropic g factor components of $g_{//} = 0.2910$ and $g_\perp = 1.9973$. The CEF parameters obtained from the fit are $B_2^0 = 3.7740$, $B_4^0 = -0.2120$, and $B_4^3 = 6.3963$.

The best fit to the data significantly overestimates the intensity ratio I_2/I_1, which likely indicates some of the expected spectral weight is split and appears as part of the extra E_3 meV mode. Adding the normalized areas of the E_2 and E_3 modes ($I_2/I_1 + I_e/I_1 = 0.699$) gives a value closer to the value predicted in the best CEF model in Table II (resulting in an improved $\chi^2 = 0.0097$). It is worth commenting on the potential origins of the additional 170.5 meV E_3 mode. Spin-orbit coupling is expected to split the $J = 5/2$ multiplet from the $J = 7/2$ manifold by at least 250 meV [47],

consistent with our observation of an intermultiplet excitation at $E = 280$ meV. This considerably weakens the possibility that the extra mode at 170 meV arises from a transition into a $J = 7/2$ state. Anomalous CEF modes observed for lanthanide ions in similar crystallographic environments are often explained by invoking coupling to phonons or vibronic effects [66–72], conjectures of hydrogen embedded within the sample [73–79], or the potential presence of chemical impurities creating multiple local environments [25,69–72,79–81]. Somewhat uniquely, none of these explanations adequately explain the origin of the E_3 mode in $KCeO_2$.

First, while the Ce wave function is known to strongly couple to the lattice, typical vibronic coupling occurs when a CEF mode resides close in energy to a phonon branch. In this scenario, the phonon and CEF mode couple together to create a bound state and a splitting or broadening of a CEF mode results. This has been observed in various lanthanide materials (e.g., $CeAl_2$ [66,67], $CeCuAl_3$ [68,69], $LiYbF_4$ [70],
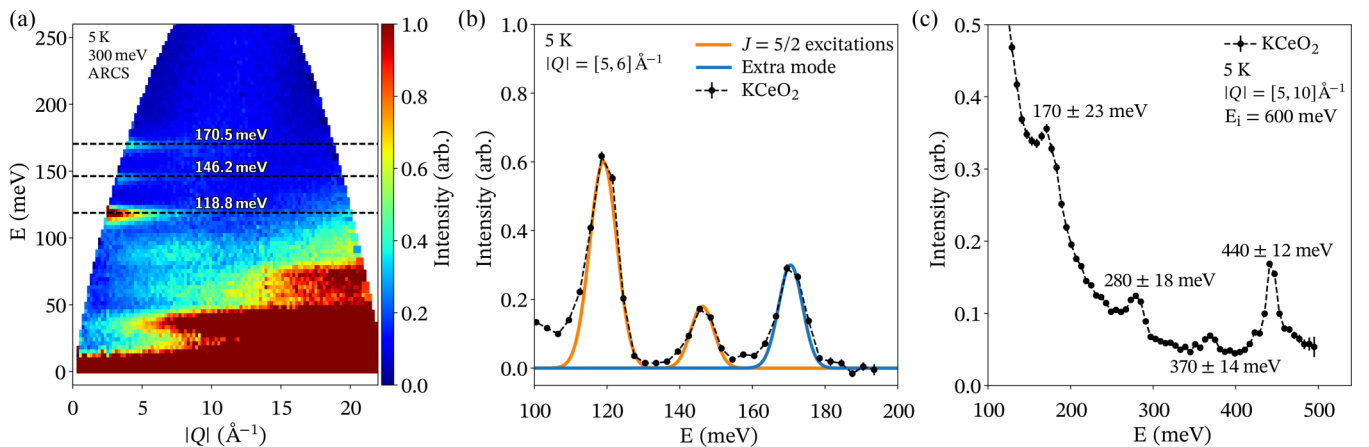

FIG. 5. (a) Momentum and energy map of neutron scattering intensities collected on the ARCS spectrometer. (b) **Q**-averaged energy cut of inelastic neutron scattering (INS) spectrum $I(\mathbf{Q}, \hbar\omega)$ collected at 5 K and $E_i = 300$ meV on the ARCS spectrometer with full width at half maximum (FWHM) energy resolution at the elastic line of 12.8 meV. A linear background is subtracted in order to determine integrated intensity ratios. (c) **Q**-averaged energy cut of $E_i = 600$ meV INS data showing the anomalous E_3 mode and the onset of transitions into the $J = 7/2$ manifold of states that begins at 280 meV. Uncertainties in energy values represent the FWHM energy resolution at each energy transfer, and error bars (often within the symbols) are uncertainty levels of 1-sigma.

TABLE II. The fit CEF wave functions for $KCeO_2$ determined from minimizing parameters extracted from $E_i = 300$ meV INS data and EPR g factor components. The energy level scheme from Eldeeb *et al.* [47] calculated with multireference configuration-interaction and spin-orbit coupling (MRCI+SOC) was used as a starting point and the 170.5 meV excitation was excluded from this analysis.

	E_1	E_2	$\frac{I_2}{I_1}$	g_{avg}	$g_\perp$	$g_{//}$	χ^2
Fit	118.8	145.7	0.639	1.6395	1.9973	0.2910	0.570
Observed	118.8	146.2	0.257	1.6340	1.9927	0.3203	

Fit wave functions:
$|\omega_{0,\pm}\rangle = 0.881| \pm 1/2\rangle + 0.473| \mp 5/2\rangle$
$|\omega_{1,\pm}\rangle = 1| \pm 3/2\rangle$
$|\omega_{3,\pm}\rangle = -0.473| \mp 1/2\rangle \mp 0.881| \pm 5/2\rangle$

and $YbPO_4$ [72]); however, the intramultiplet splitting in $KCeO_2$ is unusually high in energy, well above the single phonon cutoff apparent in our INS measurements. Additionally, phonon-induced splitting of a CEF mode typically creates two excitations above and below the unhybridized CEF energy. INS data in $KCeO_2$ resolve two CEF modes at $E_1 = 118.8$ meV and $E_2 = 146.2$ meV, each remarkably close to the calculated energies from Eldeeb *et al.* [47], strongly suggesting the $E_3 = 170.5$ meV mode is not a result of trivial splitting of either E_1 or E_2 excitations.

Second, while hydrogen impregnation is another potential source of unexplained CEF transitions in materials [73–79], the synthesis of $KCeO_2$ requires strict atmospheric handling in an inert glove box environment. A *significant* concentration of hydrogen would be required to generate the spectral weight at E_3 and is unlikely to generate the sharp energy line width observed. Related to this notion, undetected chemical impurities would arise in other experimental artifacts other than one extra INS excitation. They typically create multiple chemical environments surrounding Ce ions and generate shifted $J = 5/2$ intramultiplet excitation schemes that broaden CEF excitations or simply alter the Ce ion valence. Neither of these scenarios result in only one additional sharp CEF mode. Even a separate $J = 5/2$ Ce^{3+} environment with perfect cubic symmetry at the oxygen coordination level is expected to have a split quartet due to the farther neighbor anisotropic environment [47]. In all cases, the concentration of any secondary environment would be well within the elastic neutron scattering refinement resolution in order to create the intensity observed within the E_3 mode. In other words, the elastic neutron scattering resolution rules out chemical impurities to within 1%, and a 1% impurity could not account for the entire spectral intensity at $E_e = 170.5$ meV in INS data.

To further demonstrate this, the most likely defect state— Ce ions within the K planes—was considered via an embedded-cluster material model and quantum chemical CASSCF + SOC computations. The calculations show excited state energies at 78.5 meV and 83.5 meV due to the ligand field about the defect state. These energies are far below that of the E_3 mode, and trivial point-charge models incorporating vacancies similarly show excitation energies far below those observed experimentally. This combined with the constraints imposed by diffraction data strongly argue against localized chemical/lattice impurities as the origin of the E_3 mode.

C. Low-energy magnetic excitations

Low-energy inelastic neutron scattering data are plotted in Fig. 6, which displays both the field and temperature dependence of low-energy spin dynamics collected at 40 mK, 12 K, $\mu_0H = 0$ T, and $\mu_0H = 8$ T. Despite no resolvable magnetic Bragg peaks appearing in the elastic neutron scattering data, magnetic spectral weight appears at finite frequencies in the zero field 40 mK data near $|Q| = 1.4$ Å close to the magnetic zone centers $(1/3, 1/3, L = 0 - 4)$ for three sublattice order and with a bandwidth of roughly 1.5 meV. Using the zero field, 12 K data as an approximate paramagnetic background, subtracted data are plotted in Fig. 6(d) and reveal signatures of two spin wave branches. The first contains gapless modes dispersing up to $E = 1$ meV originating near $|Q| = 1.4$ Å, and the second appears as a gapped branch centered near 1.25 meV with a smaller bandwidth. Under an external field of $\mu_0H = 8$ T, the low energy fluctuations at 40 mK are suppressed as Ce moments begin to polarize, and the low energy gapless modes are quenched. We note here that, due to the difficulty in thermalizing powder samples, 40 mK is only the nominal temperature of the $KCeO_2$ sample in this experiment. We expect that the actual sample temperature is higher, with 100 mK being a reasonable estimate based on prior experience.

IV. DISCUSSION

Our aggregate data suggest the formation of a magnetically ordered state below 300 mK in $KCeO_2$. While an antiferromagnetic $\Theta_{CW} = -7.7$ K from Curie-Weiss analysis indicates a strong degree of magnetic frustration, a second, sharp peak in the low-temperature specific heat combined with low-energy INS data showing multibranch spin excitations at 40 mK indicate a magnetically ordered ground state. This observation is consistent with a recent report of long-range magnetic order in the sulfur-based analog $KCeS_2$ [79]. Although no new magnetic Bragg peaks were observed in elastic neutron scattering data collected at 300 mK for $KCeO_2$, the likely reason is that the ordered moment is below the limit detection in current measurements.

One naively expects that the saturated ordered moment is near the limit of detection. $NaCeO_2$, for instance, develops a $\mu = 0.57$ μ_B ordered antiferromagnetic structure below 4 K [49], suggesting an ordered moment in $KCeO_2$ of similar magnitude. Simulation of a test $120°$, $\mathbf{k} = (1/3, 1/3, 0)$ anti-
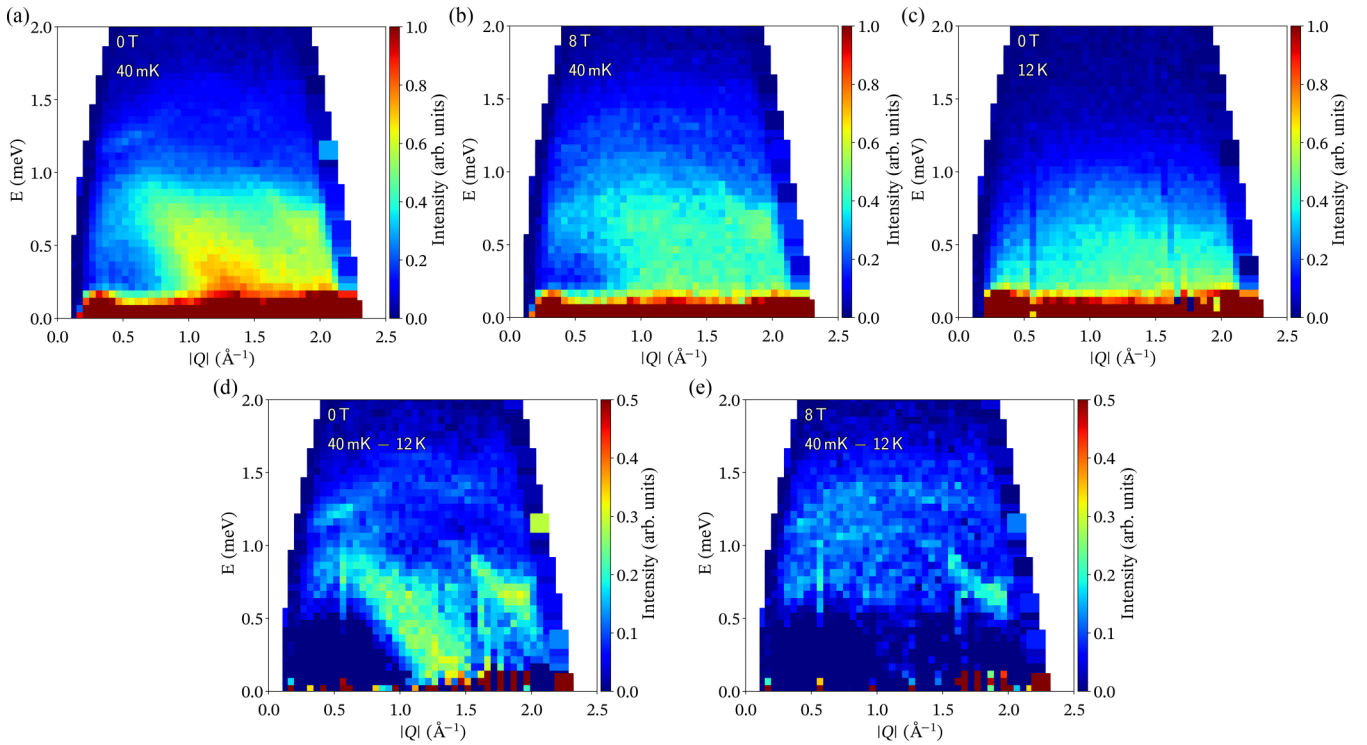
FIG. 6. Low energy inelastic neutron scattering (INS) spectra $I(\mathbf{Q}, \hbar\omega)$ collected on the CNCS spectrometer at (a) $\mu_0 H = 0$ T and 40 mK, (b) $\mu_0 H = 8$ T and 40 mK, (c) $\mu_0 H = 0$ T and 12 K. Magnetic intensity suggestive of static order originates from $\mathbf{Q} = 1.4$ Å, close to the crystallographic K point. (d) Subtracting $\mu_0 H = 0$ T and 12 K data from the data in panel (a) reveals spin-wave-like excitations in KCeO$_2$. Two distinct modes appear, the first with a bandwidth up to 1 meV from the structural K point and the second flatter mode with its spectral weight anchored close to 1.25 meV. (e) Under a field of $\mu_0 H = 8$ T, the powder-averaged modes begin to diffuse.

ferromagnetic structure with an ordered moment $\mu = 0.6\ \mu_B$ shown in Fig. 2 reveals that any magnetic Bragg scattering from this structure is outside of the current experiment's resolution and signal to noise ratio. As an upper bound, the powder averaged $g_{\text{avg}} = 1.6375$ from EPR measurements implies that the maximal ordered moment in KCeO$_2$ is only $g_{\text{avg}} J_{\text{eff}} \mu_B = 0.82\ \mu_B$. A moderate reduction from this maximal value due to quantum fluctuations or perhaps distributed intensity via short-range correlations could easily push powder-averaged magnetic scattering below the limits of detection in our current experiments.

The low-energy INS data on the other hand reveal spin-wave-like modes indicative of an ordered ground state. Unfortunately, the coarser momentum resolution of the INS measurement combined with increased background from the magnet sample environment precludes resolution of any magnetic Bragg peaks in the elastic channel of the data. The lower branch of the spin waves originates close to the K point of KCeO$_2$ expected for $\mathbf{k} = (1/3, 1/3, 0)$-type antiferromagnetic order. Though absent a direct observation of magnetic Bragg scattering, we are unable to further constrain the potential ordered state.

It is interesting to contrast the magnetic ground states of triangular lattice ARX_2 (A = alkali, R = rare earth, X = chalcogenide) systems with $S_{\text{eff}} = 1/2$ moments built from a single hole in the $4f$ shell ($R = $ Yb^{3+}) and for those built from a single electron ($R = $ Ce^{3+}). While NaYbO$_2$ shows no signs of long-range magnetic order down to 50 mK and a continuum of spin excitations resembling a quantum spin

liquid [11,28–30,32], KCeO$_2$ seemingly shows signs of ordered magnetism forming below 300 mK. Although the two compounds share an identical lattice framework of frustrated $S_{\text{eff}} = 1/2$ moments on a delafossite-based triangular lattice, the differing anisotropies of Ce^{3+} and Yb^{3+} may account for the differences in low temperature ordering. As one example, Ce^{3+} moments in KCeO$_2$ exhibit strongly anisotropic g tensors, while Yb^{3+} moments have a reduced anisotropy of $g_{//} = 1.73$ and $g_{\perp} = 3.29$ [11]. Important differences may also exist in relation to the intersite exchange anisotropies, as a result of different dominant superexchange processes in the case of $f^1 - p^6 - f^1$ and $f^{13} - p^6 - f^{13}$ electron configurations. Understanding why varying the trivalent lanthanide in this $R\bar{3}m$ delafossite structure induces ordering in Ce-based variants and a quantum disordered state in Yb-based variants will require deeper investigation into the ordered state in KCeO$_2$ and related compounds such as KCeS$_2$ [79].

Trivalent Ce^{3+} ions in a D_{3d} environment are proposed to contain a dipole-octupole Kramers doublet ground state [75–78,82,83] of pure $m_j = 3/2$ character. Separate dipolar and octupolar order can occur from this unique wave function and has been proposed for both the triangular lattice [82] and pyrochlore lattice [83]. While this ground state has been observed in pyrochlores Ce$_2$Sn$_2$O$_7$ [77,78] and Ce$_2$Zr$_2$O$_7$ [75,76], it has yet to be reported on the triangular lattice where a rich phase space of states is predicted for both the octupolar and dipolar components [82].

In KCeO$_2$, such a dipole-octopole doublet is not favored and our crystal field analysis shows that the ground-state

wave function is far from a pure $m_j = 3/2$ Kramers doublet. Table II shows the CEF wave functions with the $m_j = 3/2$ Kramers doublet comprising the first excited state at $E_1 = 118.8$ meV. Instead, the ground state wave function is a normal Kramers dipole doublet with mixed $m_j = 1/2$ and $m_j = 5/2$ character, and the symmetry of the wave functions determined from our CEF analysis agrees with predictions from Eldeeb *et al.* [47]. In comparison, the pyrochlores $Ce_2Sn_2O_7$ [77,78] and $Ce_2Zr_2O_7$ [75,76] contain two extra O^{2-} anions surrounding each Ce^{3+} ion, which seemingly favor a dipole-octupole Kramers doublet ground state [47].

The excitations in $KCeO_2$, however, do reveal an anomalous mode intermediate to the end of the predicted intramultiplet $J = 5/2$ excitations and the onset of the first $J = 5/2$ to $J = 7/2$ transition. This extra Ce^{3+} D_{3d} mode is not limited to $KCeO_2$. A similar type of high energy extra CEF mode is also present in other reported materials with similar D_{3d} environments, $KCeS_2$ [79] and $Ce_2Zr_2O_7$ [75,76]. In these materials, the extra mode was relatively weak in comparison to the other two excitations, and, as a result, the extra modes were accounted for via suppositions of weak chemical impurities or hydrogen incorporation. Additionally, $Ce_2Sn_2O_7$ [77,78] reported weak extra CEF modes within the $J = 5/2$ manifold that may also be related to the origin of the single extra mode of $KCeO_2$. For $KCeO_2$, the third unaccounted excitation at $E_3 = 170.5$ meV is intense and energetically well separated from the other two excitations E_1 and E_2. Its origin remains unknown and may be linked to the extra INS modes in $KCeS_2$, $Ce_2Zr_2O_7$, and $Ce_2Sn_2O_7$, who share a common Ce^{3+} in a D_{3d} CEF environment.

One potential origin of the E_3 mode is the presence of a strong dynamic Jahn-Teller effect akin to that observed in isovalent PrO_2 [84]. Coupling to vibronic modes associated with this effect can reduce the ordered moment and redistribute magnetic intensity into localized modes not captured within static models of the CEF spectrum. The E_3 mode in $KCeO_2$, however, is reasonably sharp in energy (resolution limited), and there is no broad distribution of magnetic spectral weight elsewhere expected from coupling to an array of lattice modes. This places rather stringent constraints on a potential vibronic mechanism and merits further systematic study.

V. CONCLUSIONS

We explored the magnetic ground state of $KCeO_2$, which crystallizes in an ideal $R\bar{3}m$ triangular lattice an-

tiferromagnetic structure with $S_{eff} = 1/2$ Ce^{3+} ions. The material develops signatures of magnetic ordering below $T_N = 300$ mK. Below T_N, spin-wave-like excitations of bandwidth ≈ 1.5 meV appear in low-energy inelastic neutron scattering data and originate near $|Q| = 1.4$ Å^{-1}. High-energy inelastic neutron scattering data reveal a strong intramultiplet crystalline electric field splitting of the Ce^{3+} $J = 5/2$ states with levels identified closely matching previous calculations [47]. However, an unexplained extra local orbital excitation appears that cannot be accounted for via conventional impurity/phonon mechanisms and whose presence should be further investigated in related materials. Understanding the origin of this unconventional mode and the microscopic distinction between the ordered state in $KCeO_2$ and the quantum disordered state in $NaYbO_2$ are important questions motivating the continued exploration of ARX_2 (A = alkali, R = rare earth, X = chalcogenide) $R\bar{3}m$ materials.

[1] P. A. Lee, An end to the drought of quantum spin liquids, Science **321**, 1306 (2008).

[2] L. Balents, Spin liquids in frustrated magnets, Nature (London) **464**, 199 (2010).

[3] L. Savary and L. Balents, Quantum spin liquids: a review, Rep. Prog. Phys. **80**, 016502 (2016).

[4] W. Witczak-Krempa, G. Chen, Y. B. Kim, and L. Balents, Correlated quantum phenomena in the strong spin-orbit regime, Annu. Rev. Condens. Matter Phys. **5**, 57 (2014).

[5] Y. Zhou, K. Kanoda, and T.-K. Ng, Quantum spin liquid states, Rev. Mod. Phys. **89**, 025003 (2017).

[6] C. Broholm, R. Cava, S. Kivelson, D. Nocera, M. Norman, and T. Senthil, Quantum spin liquids, Science **367**, eaay0668 (2020).

[7] B. Bernu, C. Lhuillier, and L. Pierre, Signature of Neel Order in Exact Spectra of Quantum Antiferromagnets on Finite Lattices, Phys. Rev. Lett. **69**, 2590 (1992).

[8] L. Capriotti, A. E. Trumper, and S. Sorella, Long-Range Neel Order in the Triangular Heisenberg Model, Phys. Rev. Lett. **82**, 3899 (1999).

[9] T. Jolicoeur, E. Dagotto, E. Gagliano, and S. Bacci, Ground-state properties of the s=1/2 heisenberg antiferromagnet on a triangular lattice, Phys. Rev. B **42**, 4800 (1990).

[10] J. Iaconis, C. Liu, G. B. Halász, and L. Balents, Spin liquid versus spin orbit coupling on the triangular lattice, Sci. Post Phys. **4**, 003 (2018).

[11] M. M. Bordelon, E. Kenney, C. Liu, T. Hogan, L. Posthuma, M. Kavand, Y. Lyu, M. Sherwin, N. P. Butch, C. Brown *et al.*, Field-tunable quantum disordered ground state in the triangular-lattice antiferromagnet NaYbO$_2$, Nat. Phys. **15**, 1058 (2019).

[12] S. Hu, W. Zhu, S. Eggert, and Y.-C. He, Dirac Spin Liquid on the Spin-1/2 Triangular Heisenberg Antiferromagnet, Phys. Rev. Lett. **123**, 207203 (2019).

[13] P. W. Anderson, The resonating valence bond state in La$_2$CuO$_4$ and superconductivity, Science **235**, 1196 (1987).

[14] P. W. Anderson, Resonating valence bonds: A new kind of insulator?, Mater. Res. Bull. **8**, 153 (1973).

[15] R. Moessner and S. L. Sondhi, Resonating Valence Bond Phase in the Triangular Lattice Quantum Dimer Model, Phys. Rev. Lett. **86**, 1881 (2001).

[16] Y. Li, D. Adroja, D. Voneshen, R. I. Bewley, Q. Zhang, A. A. Tsirlin, and P. Gegenwart, Nearest-neighbour resonating valence bonds in YbMgGaO$_4$, Nat. Commun. **8**, 1 (2017).

[17] I. Kimchi, A. Nahum, and T. Senthil, Valence Bonds in Random Quantum Magnets: Theory and Application to YbMgGaO$_4$, Phys. Rev. X **8**, 031028 (2018).

[18] Y. Li, D. Adroja, P. K. Biswas, P. J. Baker, Q. Zhang, J. Liu, A. A. Tsirlin, P. Gegenwart, and Q. Zhang, Muon Spin Relaxation Evidence for the u(1) Quantum Spin-Liquid Ground State in the Triangular Antiferromagnet YbMgGaO$_4$, Phys. Rev. Lett. **117**, 097201 (2016).

[19] Y. Li, Ybmggao4: A triangular-lattice quantum spin liquid candidate, Adv. Quantum Technol. **2**, 1900089 (2019).

[20] Y. Li, S. Bachus, B. Liu, I. Radelytskyi, A. Bertin, A. Schneidewind, Y. Tokiwa, A. A. Tsirlin, and P. Gegenwart, Rearrangement of Uncorrelated Valence Bonds Evidenced by Low-Energy Spin Excitations in YbMgGaO$_4$, Phys. Rev. Lett. **122**, 137201 (2019).

[21] X. Zhang, F. Mahmood, M. Daum, Z. Dun, J. A. M. Paddison, N. J. Laurita, T. Hong, H. Zhou, N. P. Armitage, and M. Mourigal, Hierarchy of Exchange Interactions in the Triangular-Lattice Spin Liquid YbMgGaO$_4$, Phys. Rev. X **8**, 031001 (2018).

[22] Z. Zhu, P. A. Maksimov, S. R. White, and A. L. Chernyshev, Disorder-Induced Mimicry of a Spin Liquid in YbMgGaO$_4$, Phys. Rev. Lett. **119**, 157201 (2017).

[23] Y. Li, G. Chen, W. Tong, L. Pi, J. Liu, Z. Yang, X. Wang, and Q. Zhang, Rare-Earth Triangular Lattice Spin Liquid: A Single-Crystal Study of YbMgGaO$_4$, Phys. Rev. Lett. **115**, 167203 (2015).

[24] Y. Li, H. Liao, Z. Zhang, S. Li, F. Jin, L. Ling, L. Zhang, Y. Zou, L. Pi, Z. Yang *et al.*, Gapless quantum spin liquid ground state in the two-dimensional spin-1/2 triangular antiferromagnet YbMgGaO$_4$, Sci. Rep. **5**, 16419 (2015).

[25] Y. Li, D. Adroja, R. I. Bewley, D. Voneshen, A. A. Tsirlin, P. Gegenwart, and Q. Zhang, Crystalline Electric-Field Randomness in the Triangular Lattice Spin-Liquid YbMgGaO$_4$, Phys. Rev. Lett. **118**, 107202 (2017).

[26] J. A. Paddison, M. Daum, Z. Dun, G. Ehlers, Y. Liu, M. B. Stone, H. Zhou, and M. Mourigal, Continuous excitations of the triangular-lattice quantum spin liquid YbMgGaO$_4$, Nat. Phys. **13**, 117 (2017).

[27] Y.-D. Shen, Yaoand Li, H. Wo, Y. Li, S. Shen, B. Pan, Q. Wang, H. C. Walker, P. Steffens, M. Boehm, Y. Hao, D. L. Quintero-Castro, L. W. Harriger, M. D. Frontzek, L. Hao, S. Meng, Q. Zhang, G. Chen, and J. Zhao, Evidence for a spinon fermi surface in a triangular-lattice quantum-spin-liquid candidate, Nature (London) **540**, 559 (2016).

[28] M. M. Bordelon, C. Liu, L. Posthuma, P. M. Sarte, N. P. Butch, D. M. Pajerowski, A. Banerjee, L. Balents, and S. D. Wilson, Spin excitations in the frustrated triangular lattice antiferromagnet NaYbO$_2$, Phys. Rev. B **101**, 224427 (2020).

[29] M. Baenitz, P. Schlender, J. Sichelschmidt, Y. A. Onykiienko, Z. Zangeneh, K. M. Ranjith, R. Sarkar, L. Hozoi, H. C. Walker, J.-C. Orain, H. Yasuoka, J. van den Brink, H. H. Klauss, D. S. Inosov, and T. Doert, NaYbS$_2$: A planar spin-1/2 triangular-lattice magnet and putative spin liquid, Phys. Rev. B **98**, 220409(R) (2018).

[30] L. Ding, P. Manuel, S. Bachus, F. Grußler, P. Gegenwart, J. Singleton, R. D. Johnson, H. C. Walker, D. T. Adroja, A. D. Hillier, and A. A. Tsirlin, Gapless spin-liquid state in the structurally disorder-free triangular antiferromagnet NaYbO$_2$, Phys. Rev. B **100**, 144432 (2019).

[31] W. Liu, Z. Zhang, J. Ji, Y. Liu, J. Li, X. Wang, H. Lei, G. Chen, and Q. Zhang, Rare-earth chalcogenides: A large family of triangular lattice spin liquid candidates, Chin. Phys. Lett. **35**, 117501 (2018).

[32] K. M. Ranjith, D. Dmytriieva, S. Khim, J. Sichelschmidt, S. Luther, D. Ehlers, H. Yasuoka, J. Wosnitza, A. A. Tsirlin, H. Kühne, and M. Baenitz, Field-induced instability of the quantum spin liquid ground state in the jeff=1/2 triangular-lattice compound NaYbO$_2$, Phys. Rev. B **99**, 180401(R) (2019).

[33] K. M. Ranjith, S. Luther, T. Reimann, B. Schmidt, P. Schlender, J. Sichelschmidt, H. Yasuoka, A. M. Strydom, Y. Skourski, J. Wosnitza, H. Kühne, T. Doert, and M. Baenitz, Anisotropic field-induced ordering in the triangular-lattice quantum spin liquid NaYbSe$_2$, Phys. Rev. B **100**, 224417 (2019).

[34] R. Sarkar, P. Schlender, V. Grinenko, E. Haeussler, P. J. Baker, T. Doert, and H.-H. Klauss, Quantum spin liquid ground state in the disorder free triangular lattice NaYbS$_2$, Phys. Rev. B **100**, 241116(R) (2019).

[35] J. Sichelschmidt, P. Schlender, B. Schmidt, M. Baenitz, and T. Doert, Electron spin resonance on the spin-1/2 triangular magnet NaYbS$_2$, J. Phys.: Condens. Matter **31**, 205601 (2019).

[36] J. Guo, X. Zhao, S. Ohira-Kawamura, L. Ling, J. Wang, L. He, K. Nakajima, B. Li, and Z. Zhang, Magnetic-field and composition tuned antiferromagnetic instability in the quantum spin-liquid candidate NaYbO$_2$, Phys. Rev. Materials **4**, 064410 (2020).

[37] Y. Shen, C. Liu, Y. Qin, S. Shen, Y.-D. Li, R. Bewley, A. Schneidewind, G. Chen, and J. Zhao, Intertwined dipolar and multipolar order in the triangular-lattice magnet TmMgGaO$_4$, Nat. Commun. **10**, 4530 (2019).

[38] Y. Li, S. Bachus, H. Deng, W. Schmidt, H. Thoma, V. Hutanu, Y. Tokiwa, A. A. Tsirlin, and P. Gegenwart, Partial Up-Up-Down Order with the Continuously Distributed Order Parameter in the Triangular Antiferromagnet TmMgGaO$_4$, Phys. Rev. X **10**, 011007 (2020).

[39] F. A. Cevallos, K. Stolze, T. Kong, and R. Cava, Anisotropic magnetic properties of the triangular plane lattice material TmMgGaO$_4$, Mater. Res. Bull. **105**, 154 (2018).

[40] M. M. Bordelon, C. Liu, L. Posthuma, E. Kenney, M. J. Graf, N. P. Butch, A. Banerjee, S. Calder, L. Balents, and S. D. Wilson, Frustrated heisenberg $J_1 - J_2$ model within the stretched diamond lattice of $LiYbO_2$, Phys. Rev. B **103**, 014420 (2021).

[41] Y. Hashimoto, M. Wakeshima, K. Matsuhira, Y. Hinatsu, and Y. Ishii, Structures and magnetic properties of ternary lithium oxides $LiRO_2$ (R= rare earths), Chem. Mater. **14**, 3245 (2002).

[42] Y. Hashimoto, M. Wakeshima, and Y. Hinatsu, Magnetic properties of ternary sodium oxides $NaLnO_2$ (Ln= rare earths), J. Solid State Chem. **176**, 266 (2003).

[43] B. Dong, Y. Doi, and Y. Hinatsu, Structure and magnetic properties of ternary potassium lanthanide oxides $KLnO_2$ (Ln= Y, Nd, Sm–Lu), J. Alloys Compd. **453**, 282 (2008).

[44] J. R. Cantwell, I. P. Roof, M. D. Smith, and H.-C. zur Loye, Crystal growth and optical properties of lithium–lanthanide oxides: $LiLnO_2$ (Ln= Nd, Sm, Eu, Gd and Dy), Solid State Sci. **13**, 1006 (2011).

[45] J. Xing, L. D. Sanjeewa, J. Kim, G. R. Stewart, M.-H. Du, F. A. Reboredo, R. Custelcean, and A. S. Sefat, Crystal synthesis and frustrated magnetism in triangular lattice $CsRESe_2$ (RE = La-Lu): Quantum spin liquid candidates cscese2 and csybse2, ACS Materials Letters **2**, 71 (2020).

[46] J. Fábry, L. Havlák, M. Dušek, P. Vaněk, J. Drahokoupil, and K. Jurek, Structure determination of klas2, kprs2, keus2, kgds2, klus2, kys2, rbys2, nalas2 and crystal-chemical analysis of the group 1 and thallium (i) rare-earth sulfide series, Acta Crystallographica Section B: Structural Science, Crystal Engineering and Materials **70**, 360 (2014).

[47] M. S. Eldeeb, T. Petersen, L. Hozoi, V. Yushankhai, and U. K. Rößler, Energy scales in $4f^1$ delafossite magnets: Crystal-field splittings larger than the strength of spin-orbit coupling in $KCeO_2$, Phys. Rev. Materials **4**, 124001 (2020).

[48] R. Clos, M. Devalette, C. Fouassier, and P. Hagenmuller, Sur deux nouveaux oxydes doubles $KCeO_2$ et $KPrO_2$ a structure $NaFeO_2\alpha$. les solutions solides k1+x3priii1-xpriv2x3o2, Mater. Res. Bull. **5**, 179 (1970).

[49] M. M. Bordelon, J. D. Bocarsly, L. Posthuma, A. Banerjee, Q. Zhang, and S. D. Wilson, Antiferromagnetism and crystalline electric field excitations in tetragonal $NaCeO_2$, Phys. Rev. B **103**, 024430 (2021).

[50] D. Wu, X. Li, B. Xu, N. Twu, L. Liu, and G. Ceder, $NaTiO_2$: a layered anode material for sodium-ion batteries, Energy & Environmental Science **8**, 195 (2015).

[51] J. Rodríguez-Carvajal, Recent advances in magnetic structure determination by neutron powder diffraction, Physica B **192**, 55 (1993).

[52] A. C. Larson and R. B. Von Dreele, General structural analysis system (GSAS), Report LAUR 86-748, Los Alamos National Laboratory, Los Alamos, NM, 2004.

[53] B. H. Toby, Expgui, a graphical user interface for gsas, J. Appl. Crystallogr. **34**, 210 (2001).

[54] S. Stoll and A. Schweiger, Easyspin, a comprehensive software package for spectral simulation and analysis in epr, J. Magn. Reson. **178**, 42 (2006).

[55] T. Helgaker, P. Jørgensen, and J. Olsen, *Molecular Electronic-Structure Theory* (Wiley, Chichester, 2000).

[56] M. Dolg, H. Stoll, and H. Preuss, Energy-adjusted *ab initio* pseudopotentials for the rare earth elements, J. Chem. Phys. **90**, 1730 (1989).

[57] X. Cao and M. Dolg, Segmented contraction scheme for small-core lanthanide pseudopotential basis sets, J. Mol. Struct. (Theochem) **581**, 139 (2002).

[58] W. A. de Jong, R. J. Harrison, and D. A. Dixon, Parallel Douglas-Kroll energy and gradients in NWChem: Estimating scalar relativistic effects using Douglas-Kroll contracted basis sets, J. Chem. Phys. **114**, 48 (2001).

[59] M. Dolg, H. Stoll, A. Savin, and H. Preuss, Energy-adjusted pseudopotentials for the rare earth elements, Theor. Chim. Acta **75**, 173 (1989).

[60] M. Dolg, H. Stoll, and H. Preuss, A combination of quasirelativistic pseudopotential and ligand field calculations for lanthanoid compounds, Theor. Chim. Acta **85**, 441 (1993).

[61] P. Fuentealba, H. Preuss, H. Stoll, and L. von Szentpaly, A proper account of core-polarization with pseudopotentials: single valence-electron alkali compounds, Chem. Phys. Lett. **89**, 418 (1982).

[62] A. Berning, M. Schweizer, H.-J. Werner, P. J. Knowles, and P. Palmieri, Spin-orbit matrix elements for internally contracted multireference configuration interaction wavefunctions, Mol. Phys. **98**, 1823 (2000).

[63] H. J. Werner, P. J. Knowles, G. Knizia, F. R. Manby, and M. Schütz, Molpro: a general-purpose quantum chemistry program package, Wiley Rev: Comput. Mol. Sci. **2**, 242 (2012).

[64] K. Stevens, Matrix elements and operator equivalents connected with the magnetic properties of rare earth ions, Proc. Phys. Soc. London Sect. A **65**, 209 (1952).

[65] O. Arnold, J.-C. Bilheux, J. Borreguero, A. Buts, S. I. Campbell, L. Chapon, M. Doucet, N. Draper, R. F. Leal, M. Gigg *et al.*, Mantid-data analysis and visualization package for neutron scattering and μ sr experiments, Nuclear Instruments and Methods in Physics Research Section A: Accelerators, Spectrometers, Detectors and Associated Equipment **764**, 156 (2014).

[66] P. Thalmeier and P. Fulde, Bound State between a Crystal-Field Excitation and a Phonon in $CeAl_2$, Phys. Rev. Lett. **49**, 1588 (1982).

[67] P. Thalmeier, Theory of the bound state between phonons and a cef excitation in $CeAl_2$, J. Phys. C **17**, 4153 (1984).

[68] P. Čermák, A. Schneidewind, B. Liu, M. M. Koza, C. Franz, R. Schönmann, O. Sobolev, and C. Pfleiderer, Magnetoelastic hybrid excitations in $CeAuAl_3$, Proc. Natl. Acad. Sci. **116**, 6695 (2019).

[69] D. T. Adroja, A. del Moral, C. de la Fuente, A. Fraile, E. A. Goremychkin, J. W. Taylor, A. D. Hillier, and F. Fernandez-Alonso, Vibron Quasibound State in the Noncentrosymmetric Tetragonal Heavy-Fermion Compound $CeCuAl_3$, Phys. Rev. Lett. **108**, 216402 (2012).

[70] P. Babkevich, A. Finco, M. Jeong, B. Dalla Piazza, I. Kovacevic, G. Klughertz, K. W. Krämer, C. Kraemer, D. T. Adroja, E. Goremychkin, T. Unruh, T. Strässle, A. Di Lieto, J. Jensen, and H. M. Rønnow, Neutron spectroscopic study of crystal-field excitations and the effect of the crystal field on dipolar magnetism in $LiRF_4$ (r=(Gd, Ho, Er, Tm, and Yb), Phys. Rev. B **92**, 144422 (2015).

[71] A. Ellens, H. Andres, M. L. H. ter Heerdt, R. T. Wegh, A. Meijerink, and G. Blasse, Spectral-line-broadening study of the trivalent lanthanide-ion series.ii. the variation of the electron-phonon coupling strength through the series, Phys. Rev. B **55**, 180 (1997).

[72] C.-K. Loong, M. Loewenhaupt, J. C. Nipko, M. Braden, and L. A. Boatner, Dynamic coupling of crystal-field and phonon states in $YbPO_4$, Phys. Rev. B **60**, R12549 (1999).

[73] J. Rush, J. Rowe, and A. Maeland, Neutron scattering study of hydrogen vibrations in polycrystal and glassy TiCuH, J. Phys. F **10**, L283 (1980).

[74] S. Wirth, R. Skomski, and J. M. D. Coey, Hydrogen in R_2Fe_{17} intermetallic compounds: Structural, thermodynamic, and magnetic properties, Phys. Rev. B **55**, 5700 (1997).

[75] J. Gaudet, E. M. Smith, J. Dudemaine, J. Beare, C. R. C. Buhariwalla, N. P. Butch, M. B. Stone, A. I. Kolesnikov, G. Xu, D. R. Yahne, K. A. Ross, C. A. Marjerrison, J. D. Garrett, G. M. Luke, A. D. Bianchi, and B. D. Gaulin, Quantum Spin Ice Dynamics in the Dipole-Octupole Pyrochlore Magnet $Ce_2Zr_2O_7$, Phys. Rev. Lett. **122**, 187201 (2019).

[76] B. Gao, T. Chen, D. W. Tam, C.-L. Huang, K. Sasmal, D. T. Adroja, F. Ye, H. Cao, G. Sala, M. B. Stone *et al.*, Experimental signatures of a three-dimensional quantum spin liquid in effective spin-1/2 $Ce_2Zr_2O_7$ pyrochlore, Nat. Phys. **15**, 1052 (2019).

[77] R. Sibille, N. Gauthier, E. Lhotel, V. Porée, V. Pomjakushin, R. A. Ewings, T. G. Perring, J. Ollivier, A. Wildes, C. Ritter *et al.*, A quantum liquid of magnetic octupoles on the pyrochlore lattice, Nat. Phys. **16**, 546 (2020).

[78] R. Sibille, E. Lhotel, V. Pomjakushin, C. Baines, T. Fennell, and M. Kenzelmann, Candidate Quantum Spin Liquid in the Ce^{3+} Pyrochlore Stannate $Ce_2Sn_2O_7$, Phys. Rev. Lett. **115**, 097202 (2015).

[79] G. Bastien, B. Rubrecht, E. Haeussler, P. Schlender, Z. Zangeneh, S. Avdoshenko, R. Sarkar, A. Alfonsov, S. Luther, Y. A. Onykiienko *et al.*, Long-range magnetic order in the s= 1/2 triangular lattice antiferromagnet $KCeS_2$, SciPost Phys. **9**, 041 (2020).

[80] J. Gaudet, D. D. Maharaj, G. Sala, E. Kermarrec, K. A. Ross, H. A. Dabkowska, A. I. Kolesnikov, G. E. Granroth, and B. D. Gaulin, Neutron spectroscopic study of crystalline electric field excitations in stoichiometric and lightly stuffed $Yb_2Ti_2O_7$, Phys. Rev. B **92**, 134420 (2015).

[81] J. Gaudet, A. M. Hallas, A. I. Kolesnikov, and B. D. Gaulin, Effect of chemical pressure on the crystal electric field states of erbium pyrochlore magnets, Phys. Rev. B **97**, 024415 (2018).

[82] Y.-D. Li, X. Wang, and G. Chen, Hidden multipolar orders of dipole-octupole doublets on a triangular lattice, Phys. Rev. B **94**, 201114(R) (2016).

[83] Y.-D. Li and G. Chen, Symmetry enriched u(1) topological orders for dipole-octupole doublets on a pyrochlore lattice, Phys. Rev. B **95**, 041106 (2017).

[84] A. T. Boothroyd, C. H. Gardiner, S. J. S. Lister, P. Santini, B. D. Rainford, L. D. Noailles, D. B. Currie, R. S. Eccleston, and R. I. Bewley, Localized $4f$ States and Dynamic Jahn-Teller Effect in PrO_2, Phys. Rev. Lett. **86**, 2082 (2001).